IEEE Access
Multidisciplinary | Rapid Review | Open Access Journal

Received July 23, 2019, accepted August 25, 2019, date of publication August 30, 2019, date of current version September 13, 2019.

Digital Object Identifier 10.1109/ACCESS.2019.2938452

Quantitative Reconstruction of Dual K-Edge Contrast Agent Distribution for Photon-Counting Computed Tomography

XIAOTONG ZHANG, DAYU XIAO, AND YAN KANG

College of Medicine and Biological Information Engineering, Northeastern University, Shenyang 110819, China
Engineering Research Center of Medical Imaging and Intelligent Analysis, Ministry of Education, Northeastern University, Shenyang, China

Corresponding author: Yan Kang (kangyan@bmie.neu.edu.cn)

ABSTRACT Contrast-enhanced Computed Tomography (CT) imaging is very helpful for the detection of tumor metastasis and cancer cells. It is one of the most effective means of clinical imaging examination. The objective of this paper is to realize the quantitative reconstruction of two contrast agents at the same time and obtain the non-contrast-enhanced images in four energy bins as an additional product. This paper presents an iterative material decomposition method based on volume conservation and K-edge characteristics. Compared with other K-edge based material decomposition algorithms, the proposed method can simultaneously quantify the two contrast agents and make better use of the energy information provided by the photon-counting detector. The proposed algorithm was compared with the image-domain K-edge subtraction, Angular Rejection and filtered back projection (FBP) reconstruction. Numerical simulation and Monte Carlo simulation were used to verify the effectiveness of the proposed algorithm. We found that the proposed algorithm has higher efficiency and is meaningful for the quantification of contrast agent concentration. The proposed algorithm can achieve the quantitative separation of dual K-edge contrast agent by a single scan, which is significant for reducing the radiation dose to patients and improving the efficiency of material decomposition.

INDEX TERMS Contrast-enhanced imaging, K-edge, photon-counting CT, material decomposition.

I. INTRODUCTION

Contrast-enhanced imaging based on spectral CT is an important tool for clinical diagnosis, enhancing the detection of tumor metastases and infarcted myocardium as well as determining plaque composition [1], [2], and it is of great significance for the prevention of major diseases. Depending on the attenuation characteristics of contrast agents at various energies, contrast-enhanced imaging clearly distinguishes lesion from healthy tissue [3].

When the energy of the incident X-ray photon passing through high-Z material is exactly equal to the K-edge energy of the material, the attenuation coefficient of the X-ray will rise suddenly. The K-edge property of high-Z materials gives photon-counting CT great potential in the field of contrast-enhanced imaging.

At present, dual-energy CT based on energy integral detector is widely used in clinical contrast-enhanced imaging [4]. Conventional CT based on energy integral detectors has no energy resolution ability; therefore, it cannot take advantage of K-edge characteristics of materials for imaging [5], [6]. Compared with traditional CT, dual-energy CT introduces energy information into imaging. However, sequential injection of gadolinium- and iodine- based contrast agents is often required for enhanced imaging in clinical examination. For example, the standard CT scan protocol for the liver usually includes enhanced scan of arteries and portal veins, as well as non-enhanced scan if necessary [7]. This scanning protocol is useful for studing dynamic phases in different liver pathology setting [7]. Therefore, it is meaningful to implement the material decomposition algorithm suitable for the dual-contrast single-scan CT protocol. Dual-energy CT could only obtain the projection of two energy bins at a single scan. For dual-energy CT, at least two scans are needed to distinguish the two contrast agents, increasing the radiation dose received by patients. Photon-counting CT could obtain the projection of multiple energy bins simultaneously by setting multiple energy thresholds at a single scan [8], [9].

The associate editor coordinating the review of this article and approving it for publication was Qiangqiang Yuan.

Spectral photon-counting CT could distinguish at least two contrast agents simultaneously in a single CT acquisition [10]. Photon-counting CT has the potential to reduce radiation dose thanks to the dual-contrast single-scan CT protocol and the multi-energy threshold of photon counting detector [8], [11]–[14]. To make full use of the energy information provided by the photon-counting detector, it is necessary to study the K-edge based material decomposition algorithm suitable for spectral CT.

Some studies have reported the K-edge imaging method for spectral photon-counting CT. E Roessl and R Proksa suggested that the attenuation coefficient of material was a linear combination of photoelectric effect, Compton effect and K-edge absorption, and the maximum likelihood estimation was used in the projection domain for material decomposition [15]. E Rubenstein et al. proposed to subtract the reconstructed image before the K-edge from the reconstructed image after the K-edge to highlight the contrast agent and suppress the interference of background noise [16], [17]. These are two methods for K-edge material decomposition in the projection domain and image domain;however, both only effectively distinguish one contrast agent. If two contrast agents are introduced into the method proposed by E Roessl, the increase in the number of unknown variables would introduce difficulties for obtaining the exact solution, and the reconstructed image would be noisy. Although there are some studies on K-edge material decomposition based on photon-counting CT, few methods focus on the problem of distinguishing two or more K-edge contrast agents at the same time.

In this paper, an iterative material decomposition algorithm was proposed according to the K-edge attenuation characteristics of materials at different energies. The advantage of the proposed algorithm is that the concentration distribution of two contrast agents and the non-contrast-enhanced image in four energy bins could be simultaneously obtained. The projections of different energy required by the experiments were obtained using numerical simulation and Monte Carlo simulation. The method of numerical simulation is described in the third part of the paper. Monte Carlo simulation was performed using GATE [18], an open source software based on Geant4 [19], [20]. The scanning parameters set in GATE are described in the third part. Three experiments were designed to verify the proposed algorithm, and the experimental results were compared with the results of K-edge subtraction and Angular Rejection [21].

II. METHODOLOGY

When the energy of incident photon is exactly equal to the binding energy of K-shell electrons of the material, the linear attenuation coefficient increases abruptly, and the energy value is the K-edge of the material. According to the NIST [22] table, the K-edge of iodine is 33.2 KeV and that of gadolinium is 50.2 KeV. Fig. 1 shows the mass attenuation coefficient of iodine and gadolinium. In the paper, the energy spectrum of the whole range was divided into four energy

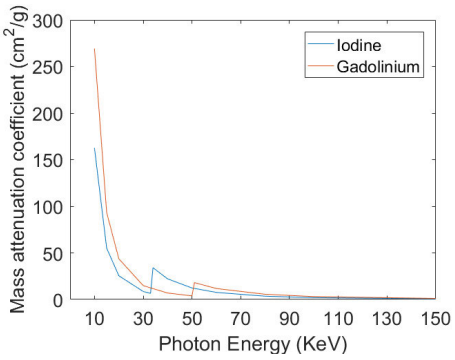

FIGURE 1. Mass attenuation coefficients of iodine and gadolinium at different energies.

ranges. We used ω_{L_1} and ω_{H_1} to represent the energy bins before and after the K-edge of iodine, respectively, and similarly, ω_{L_2} and ω_{H_2} were used to express the energy bins before and after the K-edge of gadolinium, respectively.

According to the Beer-Lambert law, the theoretical number of photons received by detector in the energy bins of ω_{L_1}, ω_{H_1}, ω_{L_2} and ω_{H_2} could be expressed as follows:

$$I_{L_1} = \int_{\omega_{L_1}} I_0(E) \times e^{-\int \mu(l,E)dl} dE \tag{1}$$

$$I_{H_1} = \int_{\omega_{H_1}} I_0(E) \times e^{-\int \mu(l,E)dl} dE \tag{2}$$

$$I_{L_2} = \int_{\omega_{L_2}} I_0(E) \times e^{-\int \mu(l,E)dl} dE \tag{3}$$

$$I_{H_2} = \int_{\omega_{H_2}} I_0(E) \times e^{-\int \mu(l,E)dl} dE \tag{4}$$

where $I_0(E)$ represents the number of incident photons at energy E, and $\mu(l, E)$ represents the linear attenuation coefficient of the scanned phantom at energy E. To show the difference in the attenuation characteristics of the contrast agent in different energy bins, the projection obtained after the K-edge was subtracted from the projection obtained before the K-edge. The attenuation coefficient of the substance in the narrow energy bin around the K-edge does not change significantly. To simplify the calculation process, the average attenuation in the energy bins of ω_{L_1}, ω_{H_1}, ω_{L_2} and ω_{H_2} was used to replace the attenuation at each energy. The projection difference of the iodine-based contrast agent could be obtained from (1) and (2):

$$\ln I_{L_1} - \ln I_{H_1} \approx \ln \frac{e^{-\int \overline{\mu}_{L_1}(l,\omega_{L_1})dl} \times \int_{\omega_{L_1}} I_0(E)dE}{e^{-\int \overline{\mu}_{H_1}(l,\omega_{H_1})dl} \times \int_{\omega_{H_1}} I_0(E)dE} \tag{5}$$

where $\overline{\mu}_{L_1}(l, \omega_{L_1})$ is the effective attenuation coefficient of the scanned object in ω_{L_1}, and $\overline{\mu}_{H_1}(l, \omega_{H_1})$ is the effective attenuation coefficient of the scanned object in ω_{H_1}. The projection difference of gadolinium-based contrast agent could

be obtained from (3) and (4):

$$\ln I_{L_2} - \ln I_{H_2} \approx \ln \frac{e^{-\int \overline{\mu}_{L_2}(l,\omega_{L_2})dl} \times \int_{\omega_{L_2}} I_0(E)dE}{e^{-\int \overline{\mu}_{H_2}(l,\omega_{H_2})dl} \times \int_{\omega_{H_2}} I_0(E)dE} \tag{6}$$

where $\overline{\mu}_{L_2}(l, \omega_{L_2})$ is the effective attenuation coefficient of the scanned object in ω_{L_2}, and $\overline{\mu}_{H_2}(l, \omega_{H_2})$ is the effective attenuation coefficient of the scanned object in ω_{H_2}.

Equations (5) and (6) could also be expressed as follows:

$$\ln \frac{I_{L_1}}{I_{H_1}} = \ln \frac{\int_{\omega_{L_1}} I_0(E)dE}{\int_{\omega_{H_1}} I_0(E)dE} + \int \overline{\mu}_{H_1}(l, \omega_{H_1})dl - \int \overline{\mu}_{L_1}(l, \omega_{L_1})dl \tag{7}$$

$$\ln \frac{I_{L_2}}{I_{H_2}} = \ln \frac{\int_{\omega_{L_2}} I_0(E)dE}{\int_{\omega_{H_2}} I_0(E)dE} + \int \overline{\mu}_{H_2}(l, \omega_{H_2})dl - \int \overline{\mu}_{L_2}(l, \omega_{L_2})dl \tag{8}$$

According to the principle of volume conservation, the attenuation coefficient of the mixture could be expressed linearly as follows:

$$\begin{cases} \mu_{mix}(l, E) = f_I(l)\mu_I(E) + f_{Gd}(l)\mu_{Gd}(E) + f_n(l)\mu_n(l, E) \\ f_n(l) = 1 - f_I(l) - f_{Gd}(l) \end{cases} \tag{9}$$

where $f_I(l)$ and $f_{Gd}(l)$ are the volume fraction of iodine-based contrast and gadolinium-based contrast agent, respectively; $\mu_I(E)$ and $\mu_{Gd}(E)$ are the linear attenuation coefficient of the two contrast agents; and $\mu_n(l, E)$ is the linear attenuation coefficient of the non-contrast-enhanced image. According to equation (9), the average attenuation in the four energy bins of ω_{L_1}, ω_{H_1}, ω_{L_2} and ω_{H_2} could be written as follows:

$$\overline{\mu}_{L_1}(l, \omega_{L_1}) = f_I(l)\overline{\mu}_I(\omega_{L_1}) + f_{Gd}(l)\overline{\mu}_{Gd}(\omega_{L_1}) + f_n(l)\overline{\mu}_n(l, \omega_{L_1}) \tag{10}$$

$$\overline{\mu}_{H_1}(l, \omega_{H_1}) = f_I(l)\overline{\mu}_I(\omega_{H_1}) + f_{Gd}(l)\overline{\mu}_{Gd}(\omega_{H_1}) + f_n(l)\overline{\mu}_n(l, \omega_{H_1}) \tag{11}$$

$$\overline{\mu}_{L_2}(l, \omega_{L_2}) = f_I(l)\overline{\mu}_I(\omega_{L_2}) + f_{Gd}(l)\overline{\mu}_{Gd}(\omega_{L_2}) + f_n(l)\overline{\mu}_n(l, \omega_{L_2}) \tag{12}$$

$$\overline{\mu}_{H_2}(l, \omega_{H_2}) = f_I(l)\overline{\mu}_I(\omega_{H_2}) + f_{Gd}(l)\overline{\mu}_{Gd}(\omega_{H_2}) + f_n(l)\overline{\mu}_n(l, \omega_{H_2}) \tag{13}$$

where $\overline{\mu}_I(\omega_{L_1})$, $\overline{\mu}_I(\omega_{H_1})$, $\overline{\mu}_{Gd}(\omega_{L_1})$, and $\overline{\mu}_{Gd}(\omega_{H_1})$ are the average attenuation of iodine-based and gadolinium-based contrast agent before and after the first K-edge (33.2 KeV). $\overline{\mu}_I(\omega_{L_2})$, $\overline{\mu}_I(\omega_{H_2})$, $\overline{\mu}_{Gd}(\omega_{L_2})$, and $\overline{\mu}_{Gd}(\omega_{H_2})$ are the average attenuation of iodine-based and gadolinium-based contrast agent before and after the second K-edge (50.2 KeV).

Substitute (10) and (11) into (7):

$$\begin{aligned} &\ln \frac{I_{L_1}}{I_{H_1}} - \ln \frac{\int_{\omega_{L_1}} I_0(E)dE}{\int_{\omega_{H_1}} I_0(E)dE} \\ &= \int (f_I(l)\overline{\mu}_I(\omega_{H_1}) + f_{Gd}(l)\overline{\mu}_{Gd}(\omega_{H_1}) + f_n(l)\overline{\mu}_n(l, \omega_{H_1}))dl \\ &\quad - \int (f_I(l)\overline{\mu}_I(\omega_{L_1}) + f_{Gd}(l)\overline{\mu}_{Gd}(\omega_{L_1}) + f_n(l)\overline{\mu}_n(l, \omega_{L_1}))dl \end{aligned} \tag{14}$$

Substitute (12) and (13) into (8):

$$\begin{aligned} &\ln \frac{I_{L_2}}{I_{H_2}} - \ln \frac{\int_{\omega_{L_2}} I_0(E)dE}{\int_{\omega_{H_2}} I_0(E)dE} \\ &= \int (f_I(l)\overline{\mu}_I(\omega_{H_2}) + f_{Gd}(l)\overline{\mu}_{Gd}(\omega_{H_2}) + f_n(l)\overline{\mu}_n(l, \omega_{H_2}))dl \\ &\quad - \int (f_I(l)\overline{\mu}_I(\omega_{L_2}) + f_{Gd}(l)\overline{\mu}_{Gd}(\omega_{L_2}) + f_n(l)\overline{\mu}_n(l, \omega_{L_2}))dl \end{aligned} \tag{15}$$

Reorganize (14) to make $f_I(l)$ and $f_{Gd}(l)$ as weighting coefficients, as shown in (16):

$$\begin{aligned} &\ln \frac{I_{L_1}}{I_{H_1}} - \ln \frac{\int_{\omega_{L_1}} I_0(E)dE}{\int_{\omega_{H_1}} I_0(E)dE} - \int (\overline{\mu}_n(l, \omega_{H_1}) - \overline{\mu}_n(l, \omega_{L_1}))dl \\ &= \int f_{Gd}(l) \times ((\overline{\mu}_{Gd}(\omega_{H_1}) - \overline{\mu}_n(l, \omega_{H_1})) \\ &\quad - (\overline{\mu}_{Gd}(\omega_{L_1}) - \overline{\mu}_n(l, \omega_{L_1})))dl \\ &\quad + \int f_I(l) \times ((\overline{\mu}_I(\omega_{H_1}) - \overline{\mu}_n(l, \omega_{H_1})) \\ &\quad - (\overline{\mu}_I(\omega_{L_1}) - \overline{\mu}_n(l, \omega_{L_1})))dl \end{aligned} \tag{16}$$

Reorganize (15) to make $f_I(l)$ and $f_{Gd}(l)$ as weighting coefficients, as shown in (17):

$$\begin{aligned} &\ln \frac{I_{L_2}}{I_{H_2}} - \ln \frac{\int_{\omega_{L_2}} I_0(E)dE}{\int_{\omega_{H_2}} I_0(E)dE} - \int (\overline{\mu}_n(l, \omega_{H_2}) - \overline{\mu}_n(l, \omega_{L_2}))dl \\ &= \int f_{Gd}(l) \times ((\overline{\mu}_{Gd}(\omega_{H_2}) - \overline{\mu}_n(l, \omega_{H_2})) \\ &\quad - (\overline{\mu}_{Gd}(\omega_{L_2}) - \overline{\mu}_n(l, \omega_{L_2})))dl \\ &\quad + \int f_I(l) \times ((\overline{\mu}_I(\omega_{H_2}) - \overline{\mu}_n(l, \omega_{H_2})) \\ &\quad - (\overline{\mu}_I(\omega_{L_2}) - \overline{\mu}_n(l, \omega_{L_2})))dl \end{aligned} \tag{17}$$

Equations (16) and (17) are the core of the algorithm proposed in this paper. Although $f_I(l), f_{Gd}(l), \overline{\mu}_n(l, \omega_{H_m})$ and $\overline{\mu}_n(l, \omega_{L_m})$ (m = 1,2) are unknown, it is possible to make $\overline{\mu}_n(l, \omega_{H_m})$ equal to $\overline{\mu}_n(l, \omega_{L_m})$ (m = 1,2); then, only two unknowns ($f_I(l)$ and $f_{Gd}(l)$) exist at the beginning of the first iteration, and the results could be easily obtained by solving the equations. The next step is to use the results of $f_I(l)$ and $f_{Gd}(l)$ to determine the remaining unknowns. The iterative process of the material decomposition method could be summarized as follows:

1. Initialize $f_I(l)$ and $f_{Gd}(l)$;
2. Load the system matrix and the projection of the four energy bins;
3. FOR iterations = 1:irt{
4. IF(iterations == 1) {
5. $\overline{\mu}_n(l, \omega_{H_m}) = \overline{\mu}_n(l, \omega_{L_m})$ m = 1,2}

TABLE 1. Brief description of scan parameters: SOD is the distance from the source to the rotation center, and SDD is the distance from the source to the detector. d_{size} is the size of the detector pixel, and α is the angle of the fanbeam. n_C is the number of channels, and n_V is the number of angular views.

	SOD (mm)	SDD (mm)	d_{Size} (mm)	α (○)	n_C	n_V
FORBILD thorax phantom	351.607	796.816	0.055	2.025	512	360
Multi-Contrast phantom	421.765	673.509	0.254	11.029	512	360
Human body phantom	570.000	940.000	0.731	52.138	1344	580

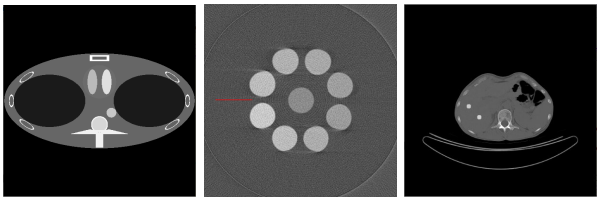

(a) (b) (c)

FIGURE 2. Phantoms used in numerical and Monte Carlo simulation. (a) The FORBILD thorax phantom with three contrast-enhanced regions. (b) The Multi-Contrast phantom. (c) The human body phantom with two contrast-enhanced regions.

6. Calculate $f_I(l)$ and $f_{Gd}(l)$:
FBP($\ln \frac{I_{Lm}}{I_{Hm}} - \ln \frac{\int_{\omega_{Lm}} I_0(E)dE}{\int_{\omega_{Hm}} I_0(E)dE} - \int(\overline{\mu}_n(l,\omega_{H_m}) - \overline{\mu}_n(l,\omega_{L_m}))dl$) m = 1,2
7. Substitute $f_I(l)$ and $f_{Gd}(l)$ into equations ((1) to (4)) to calculate $\overline{\mu}_n(l,\omega_{H_m})$ and $\overline{\mu}_n(l,\omega_{L_m})$ m = 1,2 }
8. END

III. SIMULATION

In this paper, numerical simulation and Monte Carlo simulation were used to obtain projections at different energies. The first part of this section simply describes the method of numerical simulation, and the second part describes the process of Monte Carlo simulation and lists the parameters. We adopted four energy bins (29-33 KeV, 34-38KeV, 46-50 KeV and 51-55 KeV) for both the FORBILD thorax phantom and the Multi-Contrast phantom.

A. NUMERICAL SIMULATION

In the numerical experiment, we used the FORBILD thorax phantom and the human body phantom. The left ventricle and right ventricle of FORBILD thorax phantom were injected with gadolinium-based contrast agent with concentrations of 1.5% (Gd) and 1.0% (Gd), respectively, and the artery was filled with iodine-based contrast agent with a concentration of 1.8% (I), as shown in Fig. 2(a). The human body phantom contains two ROIs with a diameter of 1.17 cm in the liver region, as shown in Fig. 2(c). The left circular area was filled with blood and iodine-based contrast agent of 0.1% (I), 0.2% (I) and 0.5% (I), while the right circular region was filled with blood and gadolinium-based contrast agent of 0.1% (Gd), 0.2% (Gd) and 0.5% (Gd). The attenuation coefficients of materials at different energies could be inquired on the NIST library. The HU range of the pixel in the image could correspond to a certain substance, which could correspond to the density and element composition. Then the monoenergetic images could be obtained by filling attenuation coefficients of different energies into the corresponding positions.

In the simulation, the system matrix was used to project monoenergetic images to obtain the monoenergetic projections:

$$P_{mono} = M \times [X_{minE}, ..., X_{maxE}] = [p_{minE}, ..., p_{maxE}] \quad (18)$$

where M is the system matrix, X are the monoenergetic images with a total of $(maxE - minE)$ energy levels, and p are monoenergetic projections. The incident X-ray spectra of 90 kVp and 130 kVp were used for FORBILD thorax phantom and human body phantom, respectively. The scan parameters of the system matrix are shown in Table 1. Formula (18) could be converted into the following:

$$exp(-P_{mono}) = [e^{-p_{minE}}, ..., e^{-p_{maxE}}] \quad (19)$$

The projection received by the photon-counting detector at different energy bins could be expressed in the form of accumulation:

$$I_{EBin} = \sum_{E=EBin} I_0(E) \times exp(-P_{mono}(E)) \quad (20)$$

where $I_0(E)$ is the number of incident photons at energy E, and I_{EBin} represents the number of photons received by the detector in the energy bin. I_{EBin} is the input of the proposed algorithm.

B. MONTE CARLO SIMULATION

Monte Carlo simulation is widely used in the field of medical imaging, which is of great help to the research of reconstruction algorithm optimization, artifact elimination and dose measurement. GATE is a software based on Geant4, which could be used for Monte Carlo simulation. In this study, we used GATE 8.1 version to simulate the CT scanning process to obtain the multi-energy projection.

We designed a photon counting detector made of CdTe in the GATE environment. The pixel size of the detector was 0.254 × 0.254. The detector was set to have 512 channels, and the number of pixels on the detector was 1 × 512. More detailed geometric parameters are listed in Table 1. SPECPRO software was used to generate a spectrum with a tube voltage of 90 kVp. The anode target angle was 12 degrees, and the thickness of aluminum filter was 2 mm.

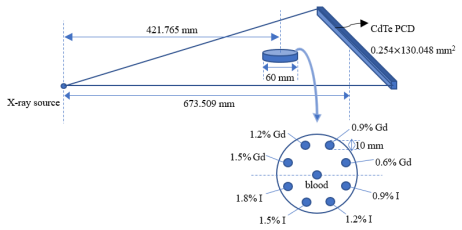

FIGURE 3. Photon-counting CT system designed in GATE environment. The multi-contrast phantom was composed of nine holes with a diameter of 10 mm filled with contrast agent of different concentrations.

The source emitted 5×10^7 photons at each projection angle. As shown in Fig. 2(b), the multi-contrast phantom had nine holes to be filled with mixed solutions of blood and contrast agents of different concentration. The concentration of the solution rotated clockwise from the red line was 1.5% (Gd), 1.2% (Gd), 0.9% (Gd), 0.6% (Gd), 1.8% (I), 1.5% (I), 1.2% (I), and 0.9% (I). The solution in the center was blood without contrast agent. Fig. 3 shows the photon-counting CT system designed based on the GATE platform.

IV. EXPERIMENTS AND RESULTS

A. PERFORMANCE EVALUATION OF ITERATIVE MATERIAL DECOMPOSITION ALGORITHM

The concentration maps of iodine-based and gadolinium-based contrast agents in the first experiment are shown in Fig. 4(a) to (c). Fig. 4(a) shows the concentration of gadolinium-based contrast agent in the left and right ventricles of FORBILD thorax phantom, and Fig. 4(b) shows the concentration of iodine-based contrast agent in the artery. Fig. 4(c) is the reconstructed image of the FORBILD thorax phantom covered with pseudo-color. The material decomposition of the multi-contrast phantom based on GATE simulation is shown in Fig. 4(d) to (f). Gadolinium map shows the material decomposition at the concentration of 1.5% (Gd), 1.2% (Gd), 0.9% (Gd) and 0.6% (Gd), as shown in Fig. 4(d). The distribution of iodine with concentrations of 1.8% (I), 1.5% (I), 1.2% (I) and 0.9% (I) is shown in Fig. 4(e). Fig. 4(f) shows the pseudo-color image of the multi-contrast phantom. The proposed algorithm could effectively distinguish the iodine solution from gadolinium solution visually, and the concentration maps of the two K-edge materials were generated simultaneously. To verify the accuracy of material decomposition results numerically, pixel values in ROI on the concentration image were displayed, as shown in Fig. 5. The pixel position was marked with red dotted lines, as shown in Fig. 4, and the yellow labels next to the marked line correspond to the serial number in Fig. 5.

The estimated concentrations calculated by the proposed algorithm fluctuate above and below the real concentration, as shown in Fig. 5. The first experiment for the FORBILD thorax phantom is a theoretical numerical simulation, in which the noise of material decomposition is small. The second experiment for the Multi-Contrast phantom is a Monte Carlo simulation, which is closer to the real CT scan but also introduces more noise.

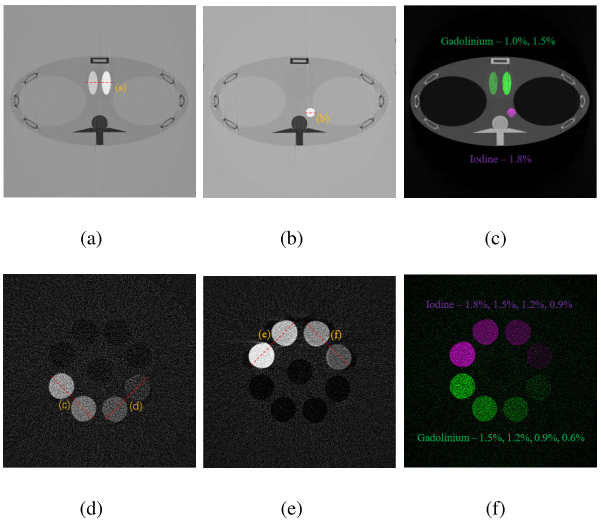

FIGURE 4. Material decomposition using the proposed algorithm. (a) Gadolinium map of FORBILD thorax phantom with the display range [−2.89, 2]. (b) Iodine map of FORBILD thorax phantom with the display range [−4.56, 2.2]. (c) Pseudo-color image of FORBILD thorax phantom. (d) Gadolinium map of multi-contrast phantom with the display range [−0.26,3.28]. (e) Iodine map of multi-contrast phantom with the display range [−0.16,1.84]. (f) Pseudo-color image of multi-contrast phantom.

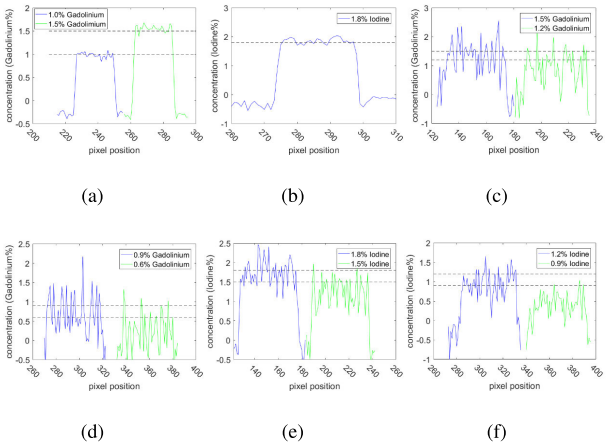

FIGURE 5. Line profiles of the FORBILD thorax phantom and multi-contrast phantom after material decomposition. The dotted lines represent the true concentration of the element. The line profiles include the following concentrations: (a) 1.5% (Gd) and 1.0% (Gd), (b) 1.8% (I), (c) 1.5% (Gd), 1.2% (Gd), (d) 0.9% (Gd), and 0.6% (Gd), (e) 1.8% (I) and 1.5% (I), (f) 1.2% (I), and 0.9% (I).

The mean, standard deviation and mean square error of the above decomposition results were also used to evaluate the performance of the algorithm, as shown in Table 2 and Table 3. From the analysis of the numerical indexes in Table 2, the proposed algorithm can achieve a good accuracy, whether for the numerical simulation or Monte Carlo simulation, that is, the estimated mean value of contrast agent concentration has little difference from the real concentration, especially when the contrast agent concentration is greater than 1.0%. Due to the consideration of photoelectric effect, Compton scattering and detector circuit noise in Monte Carlo simulation, compared with thorax phantom in ideal state, which is

TABLE 2. Mean and standard deviation of decomposition results of FORBILD thorax phantom and multi-contrast phantom.

mean± SD	1.8% (I)	1.5% (I)	1.2% (I)	0.9% (I)	1.5% (Gd)	1.2% (Gd)	1.0% (Gd)	0.9% (Gd)	0.6% (Gd)
FORBILD thorax phantom	1.8453± 0.0952	×	×	×	1.6074± 0.0646	×	0.9729± 0.0591	×	×
Multi-Contrast phantom	1.6705± 0.3314	1.2406± 0.3305	0.8777± 0.3129	0.4873± 0.2830	1.4613± 0.5298	1.0768± 0.5081	×	0.7006± 0.4404	0.4680± 0.3565

TABLE 3. Mean square error of decomposition results of FORBILD thorax phantom and multi-contrast phantom.

mean± SD	1.8% (I)	1.5% (I)	1.2% (I)	0.9% (I)	1.5% (Gd)	1.2% (Gd)	1.0% (Gd)	0.9% (Gd)	0.6% (Gd)
FORBILD thorax phantom	0.0111	×	×	×	0.0157	×	0.0042	×	×
Multi-Contrast phantom	0.1265	0.1764	0.2017	0.2504	0.2820	0.2731	×	0.2336	0.1444

not disturbed by noise, multi-contrast phantom is very close to the real scanning condition. The larger standard deviation of the decomposition result of multi-contrast phantom is caused by noise, but noise is inevitable in the case of actual scanning. The mean square error shown in Table 3 represents the difference between the decomposition results and the true concentration of contrast agent. The range of mean square error of decomposition results in the numerical simulation experiment with thorax phantom is [0.01,0.015], and the range of Monte Carlo simulation experiment with multi-contrast phantom is [0.12,0.29].

In addition, the proposed algorithm could not only achieve K-edge material decomposition but also generate non-contrast-enhanced images in different energy bins simultaneously. The estimated non-contrast-enhanced images were compared with the real non-contrast-enhanced images, and the errors between the two groups of images were accumulated according to (22):

$$error = \frac{norm_2(f_{estimate} - f_{real})}{norm_2(f_{real})} \tag{21}$$

where $f_{estimate}$ represents estimated non-contrast enhanced image, f_{real} represents real non-contrast enhanced image. The virtual non-contrast enhanced images of the third experiment for human body phantom with concentrations of 0.1% (Gd) and 0.1% (I) are shown in Fig. 6. Visually, the reconstructed tissue images are very close to the real tissue images. The errors before the first and second K-edge are 0.0167 and 0.0292, and the errors after the first and second K-edge are 0.0527 and 0.0409, respectively.

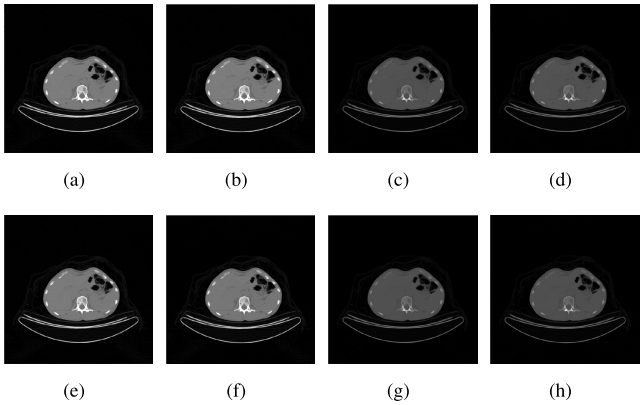

FIGURE 6. Non-contrast-enhanced images of human body phantom. (a) and (c) are the virtual non-contrast-enhanced images before the first K-edge (33.2 KeV) and the second K-edge (50.2 KeV), respectively; (b) and (d) are the virtual non-contrast-enhanced images after the first K-edge and the second K-edge, respectively; (e) and (g) are the real non-contrast-enhanced images before the first K-edge and the second K-edge, respectively; (f) and (h) are the real non-contrast-enhanced images after the first K-edge and the second K-edge, respectively. The display range is [0, 3000] HU.

B. COMPARATIVE EVALUATION

In this paper, the proposed iterative material decomposition algorithm was compared with image domain-based K-edge subtraction, angular rejection and traditional FBP reconstruction. Fig. 7 and Fig. 8 show gadolinium and iodine maps of human body phantom with concentrations of 0.1% Gd (I), 0.2% Gd (I) and 0.5% Gd (I). As shown in Fig. 7 and Fig. 8, the first, second and third lines are the results of iterative material decomposition, K-edge subtraction and angular rejection respectively. The FBP reconstruction is shown in the last line.

K-edge subtraction in the image domain is an effective and widely used method to distinguish K-edge materials, but its limitations are that it is unable to distinguish two contrast agents at the same time, and it is difficult to achieve accurate concentration quantification. According to the experimental results of human body phantom, the effect of the proposed algorithm is very close to that of K-edge subtraction, and both are significantly better than traditional CT reconstruction. Especially in the case of low concentration, the traditional CT images can barely highlight the area with contrast agent, and different contrast agents with similar density cannot be distinguished by the grayscale of the image.

The image-based K-edge substraction is difficult to quantify the concentration of contrast agent. To comprehensively discuss the performance of iterative material decomposition

TABLE 4. Mean and standard deviation in ROI of material maps generated by the proposed algorithm and angular rejection algorithm in the human body phantom experiment.

mean± SD	0.5% (Gd)	0.2% (Gd)	0.1% (Gd)	0.5% (I)	0.2% (I)	0.1% (I)
proposed algorithm	0.5143± 0.0065	0.1941± 0.0027	0.0879± 0.0015	0.4868± 0.0054	0.1679± 0.0027	0.0617± 0.0020
Angular rejection algorithm	0.5018± 0.0079	0.4501± 0.0088	0.4330± 0.0091	0.5015± 0.0077	0.4561± 0.0082	0.4410± 0.0081

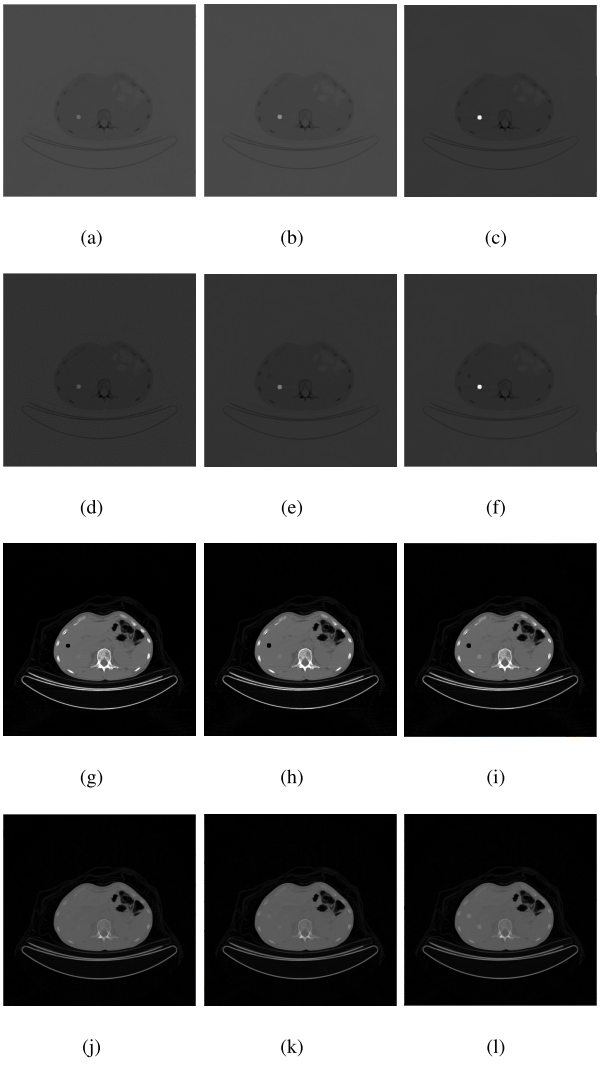

FIGURE 7. Comparison of gadolinium maps with different algorithms. (a)-(c) show iterative material decomposition images of human body phantom with concentrations of 0.1% (Gd), 0.2% (Gd) and 0.5% (Gd); (d)-(f) show K-edge subtraction images of human body phantom with concentrations of 0.1% (Gd), 0.2% (Gd) and 0.5% (Gd); (g)-(i) are the material decomposition images with concentrations of 0.1% (Gd), 0.2% (Gd) and 0.5% (Gd) generated by Angular Rejection; (j)-(l) show conventional CT images of human body phantom with concentrations of 0.1% (Gd), 0.2% (Gd) and 0.5% (Gd). The display ranges are [-0.02, 0.05] for (a)-(c), [-1.94e-4, 7.81e-4] for (d)-(f), [0,1.0] for (g)-(i), [0, 3000] HU for (j)-(l).

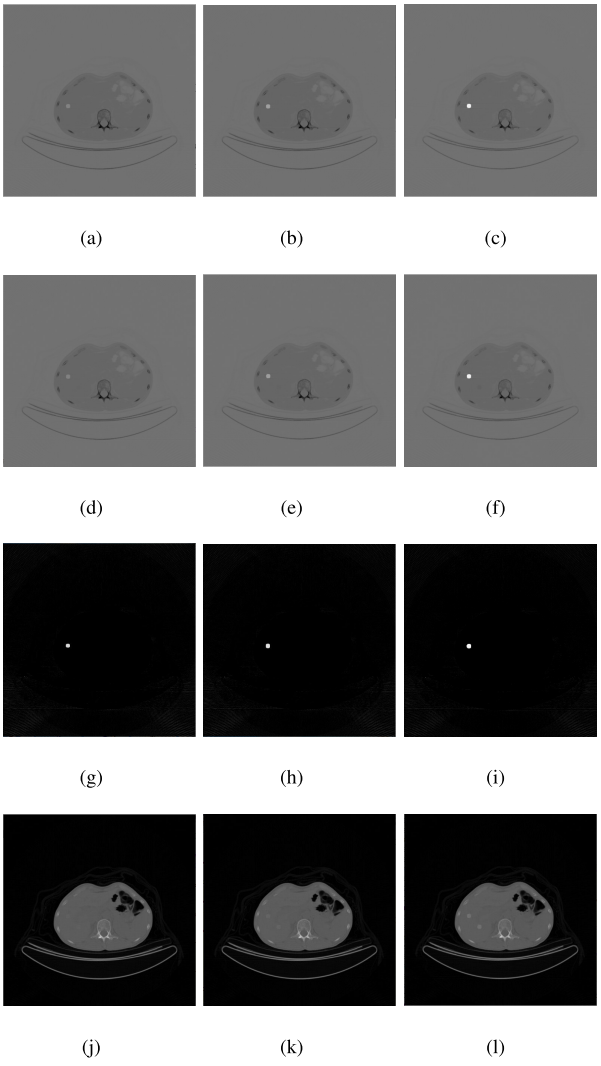

FIGURE 8. Comparison of iodine maps with different algorithms. (a)-(c) show iterative material decomposition images of human body phantom with concentrations of 0.1% (I), 0.2% (I) and 0.5% (I); (d)-(f) show K-edge subtraction images of human body phantom with concentrations of 0.1% (I), 0.2% (I) and 0.5% (I); (g)-(i) are the material decomposition images with concentrations of 0.1% (I), 0.2% (I) and 0.5% (I) generated by Angular Rejection; (j)-(l) show conventional CT images of human body phantom with concentrations of 0.1% (I), 0.2% (I) and 0.5% (I). The display ranges are [-0.04, 0.05] for (a)-(c), [-1.17e-3, 1.46e-3] for (d)-(f), [0,0.52] for (g)-(i), [0, 3000] HU for (j)-(l).

algorithm, the angular rejection [21] algorithm is also used as a comparative experiment. Angular rejection is a material decomposition method used by MARS [23]–[25] system. Calibration phantom with known material concentration is necessary for Angular Rejection method, which is used to obtain the effective attenuation coefficient

TABLE 5. Mean square error in ROI of material maps generated by the proposed algorithm and angular rejection algorithm in the real human phantom experiment.

MSE	0.5% (Gd)	0.2% (Gd)	0.1% (Gd)	0.5% (I)	0.2% (I)	0.1% (I)
proposed algorithm	2.4705e-4	4.1676e-5	1.4798e-4	2.0354e-4	0.0010	0.0015
Angular rejection algorithm	6.4478e-5	0.0626	0.1110	6.0331e-5	0.0656	0.1163

TABLE 6. Mean and standard deviation in ROI of material maps generated by the proposed algorithm and angular rejection algorithm in the multi-contrast phantom experiment.

mean± SD	1.5% (Gd)	1.2% (Gd)	0.9% (Gd)	0.6% (Gd)	1.8% (I)	1.5% (I)	1.2% (I)	0.9% (I)
proposed algorithm	1.4698± 0.5317	1.0757± 0.5046	0.7038± 0.4380	0.4590± 0.3541	1.6710± 0.3394	1.2338± 0.3503	0.8840± 0.3193	0.4810± 0.2824
Angular rejection algorithm	1.5033± 0.1418	1.3527± 0.1441	1.2496± 0.1443	1.1350± 0.1601	1.8008± 0.1637	1.6832± 0.1755	1.5726± 0.1652	1.3971± 0.1827

of different materials for subsequent material decomposition. In this study, reconstructed images in three energy bins (10-30 KeV, 30-50 KeV, 50-70 KeV) were adopted to realize material decomposition using Angular Rejection.

In the experiment of human phantom, the phantom containing 0.5% Gd and 0.5% I was used as the calibration phantom. As shown in Fig. 7 and Fig. 8, Angular Rejection can visually distinguish iodine-based contrast agent from background. However, gadolinium-based contrast agent cannot be separated from the background, and even at low concentration (0.1% Gd), there is little contrast between the ROI containing gadolinium-based contrast agents and the background. Since Angular Rejection can quantify the concentration of contrast agent, the proposed algorithm was also evaluated numerically, as shown in Table 4 and Table 5. According to Table 4, when the concentration of contrast agent is 0.5% Gd(I), the mean and standard deviation of iterative material decomposition are very close to those of Angular Rejection, and the mean values of both algorithms are close to the true concentrations. With the decrease of concentration, there is a big deviation between the mean value of Angular Rejection and the real concentration, which might be related to the concentration of calibration phantom. The mean value of iterative material decomposition is not affected by the concentration reduction and is still close to the real concentration, indicating that the proposed algorithm is more effective for quantifying the concentration of contrast agent. The mean square error shown in Table 5 also indicates that the iterative material decomposition algorithm has high quantization accuracy.

In the Monte Carlo simulation experiment with multi-contrast phantom, iterative material decomposition, K-edge subtraction and Angular Rejection can effectively distinguish iodine- and gadolinium-based contrast agent visually, and the contrast of material maps generated by these three methods is much better than that reconstructed by FBP, as shown in Fig. 9. In the experiment of multi-contrast phantom, Angular Rejection used calibration phantom with 1.5% Gd and 1.8% I. According to numerical evaluation in Table 6 and Table 7,

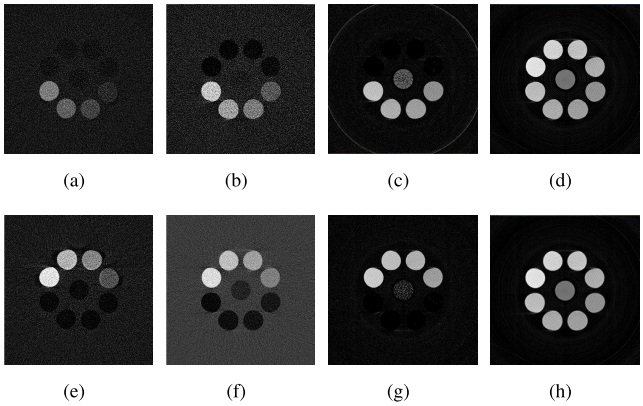

FIGURE 9. Material decomposition of multi-contrast phantom using four different algorithms. (a)-(c) are gadolinium maps with display range of [-0.26,3.28], [-0.26,3.28] and [0,2.01] obtained by iterative material decomposition, K-edge subtraction and Angular Rejection algorithm; (e)-(g) are iodine maps with display range of [-0.16,1.84], [-1.88,6.14] and [0,2.28] obtained by iterative material decomposition, K-edge subtraction and Angular Rejection algorithm; (d) and (h) are FBP reconstruction images with display range of [0,80].

Angular Rejection performs well when the contrast agent concentration is similar to that of the calibration phantom. At higher contrast agent concentrations, such as 1.5% Gd, 1.2% Gd, 1.8% I and 1.5% I, the mean values of iterative material decomposition and Angular Rejection are close to the true concentration, and the standard deviation and mean square error of Angular Rejection are smaller than those of iterative material decomposition. However, as the concentration decreases, the error of material maps generated by the Angular Rejection becomes larger. When the contrast agent concentration is low, such as 0.6% Gd and 0.9% I, the mean square error of Angular Rejection is larger than that of the iterative material decomposition. According to Fig. 7 to Fig. 9, compared with the proposed algorithm, the image-based Angular Rejection would classify tissue wrongly as contrast agent. As shown in Fig. 9, blood without contrast agent in the center of the multi-contrast phantom was incorrectly classified as contrast agent using Angular Rejection,

TABLE 7. Mean square error in ROI of material maps generated by the proposed algorithm and angular rejection algorithm in the multi-contrast phantom experiment.

MSE	1.5% (Gd)	1.2% (Gd)	0.9% (Gd)	0.6% (Gd)	1.8% (I)	1.5% (I)	1.2% (I)	0.9% (I)
proposed algorithm	0.2835	0.2717	0.2302	0.1452	0.1318	0.1935	0.2018	0.2552
Angular rejection algorithm	0.0201	0.0441	0.1430	0.3119	0.0268	0.0644	0.1661	0.2805

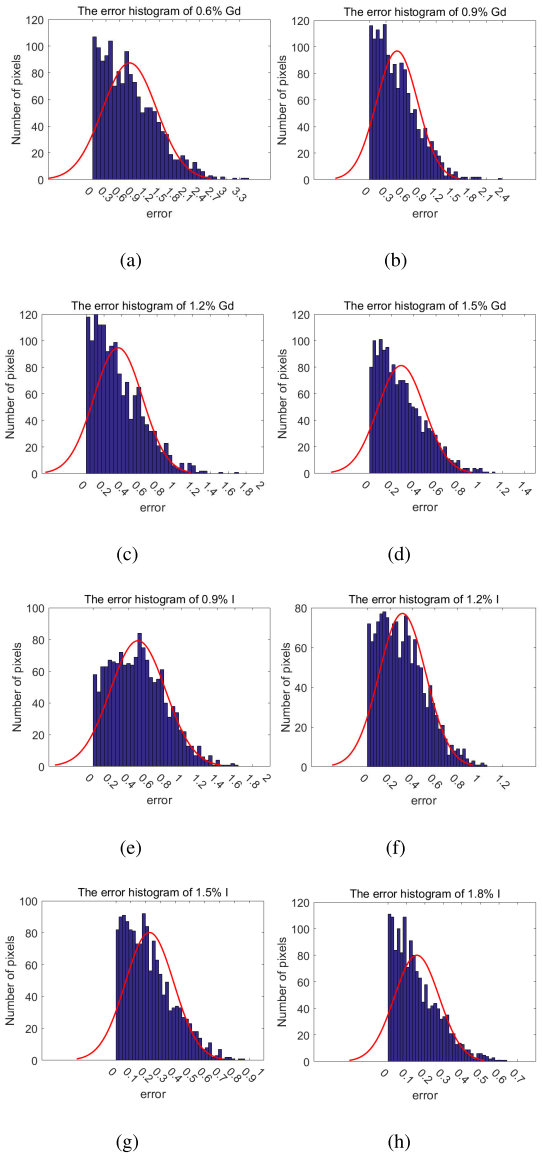

FIGURE 10. Error histogram and probability density curve of decomposition results of multi-contrast phantom. (a)-(d) represents the error histogram of gadolinium map with concentration of 0.6% (Gd), 0.9% (Gd), 1.2% (Gd), 1.5% (Gd); (e)-(h) represents the error histogram of iodine map with concentration of 0.9% (I), 1.2% (I), 1.5% (I), 1.8% (I).

whether on iodine map or gadolinium map. The accuracy of Angular Rejection is easily affected by the calibration phantom, and this image-domain-based method is sensitive to the quality of reconstructed image.

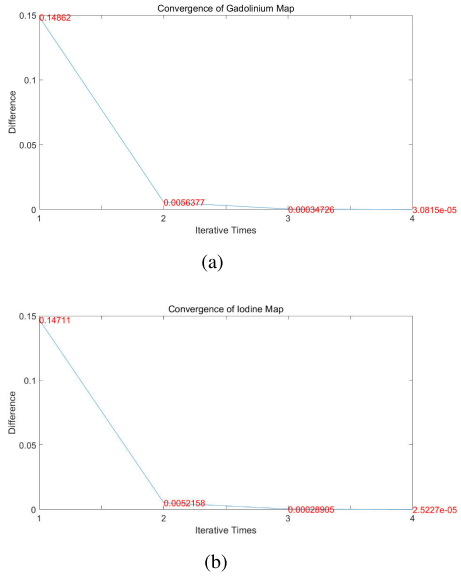

FIGURE 11. Convergence of the algorithm. For the second experiment for Multi-Contrast phantom, (a) show the difference in gadolinium distribution changed with the number of iterations; (b) show the difference in iodine distribution changed with the number of iterations.

V. DISCUSSION

Among the existing K-edge-based imaging methods, the projection decomposition proposed by E Roessl and K-edge subtraction proposed by E Rubenstein have been widely accepted. In addition to the K-edge method, Angular Rejection used by MARS system also has high precision and efficiency. The projection decomposition method uses maximum likelihood estimation to separate the contrast agent directly in the projection domain. Since the number of pixels in the projection is quite large, the maximum likelihood estimation needs to be used for the projection decomposition of each pixel, resulting in long time consumption. K-edge subtraction in the image domain clearly distinguished the contrast agent from the surrounding tissues. In clinical practice, however, this method requires a scan before the contrast agent is injected, undoubtedly increasing the radiation dose to the patient. As discussed above, Angular Rejection needs to use the calibration phantom and requires high quality of reconstructed images. Moreover, the scanning conditions of the calibration phantom must be consistent with the scanning conditions of the target object to obtain more accurate effective attenuation coefficient of the material. The method proposed in this paper distinguished two kinds of contrast agents simultaneously using a single scan, and the non-contrast-enhanced

images of four energy bins could be obtained. The iterative material decomposition algorithm made full use of the energy information provided by the photon counting detector, and the data obtained from a single scan met the requirements of material decomposition, thereby reducing the radiation dose to patients.

We also analyzed the applicability and convergence of the new algorithm. In the Monte Carlo simulation experiment with multi-contrast phantom, the error histogram and normal density curve of the error in the ROI of iodine (gadolinium) map are shown in Fig. 10. The error was calculated according to (21), where $f_{estimate}$ represents the value of a pixel on the material map and f_{real} represents the real material concentration. This error is an assessment at the pixel level rather than the material map level. Fig. 10 shows the statistics of the number of pixels in different error ranges in the ROI of the phantom. According to the analysis of Fig. 10, the errors of pixel values in ROI of iodine map and gadolinium map are normally distributed. The case in Fig. 10 where the error on the x axis is greater than 1 is caused by the negative value of the pixel. Pixels with a value less than zero belong to the category of invalid material decomposition. From the distribution of errors, the proposed algorithm can achieve more accurate decomposition results when the contrast agent concentration is higher than 1.0%. Although the proposed algorithm could distinguish the regions with lower contrast agent concentration, it would cause a large quantization error. We evaluated the convergence of the proposed iterative algorithm based on the difference between the current decomposition $f_{current}$ and the previous decomposition $f_{previous}$ in the iterative process. The difference was defined as (22):

$$difference = \frac{norm_2(f_{current} - f_{previous})}{norm_2(f_{previous})} \tag{22}$$

In the case of Multi-Contrast phantoms using Monte Carlo simulation, the difference decreases with the increase in iterative times, as shown in Fig. 11. The proposed algorithm has good convergence, and the final results could be obtained after several iterations.

VI. CONCLUSION

In this paper, we proposed a K-edge-based iterative material decomposition algorithm. This method distinguished two contrast agents simultaneously and obtained the virtual non-contrast enhanced images. The new method improves the efficiency and reduces the radiation dose. It overcomes the limitation of K-edge subtraction that distinguishes one contrast agent at a time, and the results are comparable to those of K-edge subtraction. The proposed algorithm has great potential in the field of multi-contrast-enhanced imaging.

REFERENCES

[1] R. Symons, T. E. Cork, M. N. Lakshmanan, R. Evers, C. Davies-Venn, K. A. Rice, M. L. Thomas, C.-Y. Liu, S. Kappler, S. Ulzheimer, V. Sandfort, D. A. Bluemke, and A. Pourmorteza, "Dual-contrast agent photon-counting computed tomography of the heart: Initial experience," *Int. J. Cardiovascular Imag.*, vol. 33, no. 8, pp. 1–9, 2017.

[2] A. Pourmorteza, R. Symons, V. Sandfort, M. Mallek, M. K. Fuld, G. Henderson, E. C. Jones, A. A. Malayeri, L. R. Folio, and D. A. Bluemke, "Abdominal imaging with contrast-enhanced photon-counting CT: First human experience," *Radiology*, vol. 279, no. 1, pp. 239–245, 2016.

[3] A.-K. Carton, C. Ullberg, and A. D. A. Maidment, "Optimization of a dual-energy contrast-enhanced technique for a photon-counting digital breast tomosynthesis system: II. An experimental validation," *Med. Phys.*, vol. 37, no. 11, pp. 5908–5913, 2010.

[4] H. W. Goo and J. M. Goo, "Dual-energy CT: New horizon in medical imaging," *Korean J. Radiol.*, vol. 18, no. 4, pp. 555–569, 2017.

[5] A. Macovski, R. E. Alvarez, J. L.-H. Chan, J. P. Stonestrom, and L. M. Zatz, "Energy dependent reconstruction in X-ray computerized tomography," *Comput. Biol. Med.*, vol. 6, no. 4, pp. 325–334, Oct. 1976.

[6] E. Roessl and R. Proksa, "K-edge imaging in X-ray computed tomography using multi-bin photon counting detectors," *Phys. Med. Biol.*, vol. 52, no. 15, p. 4679, 2007.

[7] D. Muenzel, H. Daerr, R. Proksa, A. A. Fingerle, F. K. Kopp, P. Douek, J. Herzen, F. Pfeiffer, E. J. Rummeny, and P. B. Noël, "Simultaneous dual-contrast multi-phase liver imaging using spectral photon-counting computed tomography: A proof-of-concept study," *Eur. Radiol. Exp.*, vol. 1, no. 1, p. 25, Dec. 2017.

[8] R. Ballabriga, M. Campbell, E. H. M. Heijne, X. Llopart, and L. Tlustos, "The Medipix3 prototype, a pixel readout chip working in single photon counting mode with improved spectrometric performance," *IEEE Trans. Nucl. Sci.*, vol. 54, no. 5, pp. 1824–1829, Oct. 2007.

[9] J. S. Iwanczyk, E. NygåRd, O. Meirav, J. Arenson, W. C. Barber, N. E. Hartsough, N. Malakhov, and J. C. Wessel, "Photon counting energy dispersive detector arrays for X-ray imaging," *IEEE Trans. Nucl. Sci.*, vol. 56, no. 3, pp. 535–542, Jun. 2009.

[10] D. Muenzel, D. Bar-Ness, E. Roessl, I. Blevis, M. Bartels, A. A. Fingerle, S. Ruschke, P. Coulon, H. Daerr, and F. K. Kopp, "Spectral photon-counting CT: Initial experience with dual–contrast agent K-edge colonography," *Radiology*, vol. 283, no. 3, pp. 723–728, 2016.

[11] K. Akiba, J. Alozy, R. Aoude, B. M. Van, J. Buytaert, P. Collins, S. A. Dosil, R. Dumps, A. Gallas, and C. A. Hombach, "Characterisation of medipix3 silicon detectors in a charged-particle beam," *J. Instrum.*, vol. 11, no. 1, Jan. 2016, Art. no. P01011.

[12] R. Ballabriga, M. Campbell, E. Heijne, X. Llopart, L. Tlustos, and W. Wong, "Medipix3: A 64 k pixel detector readout chip working in single photon counting mode with improved spectrometric performance," *Nucl. Instrum. Methods Phys. Res. A, Accel., Spectrometers, Detect. Associated Equip.*, vol. 633, no. 1, pp. S15–S18, 2011.

[13] L. F. N. D. Carramate, F. Nachtrab, M. Firsching, A. L. M. Silva, A. M. da Silva, J. F. C. A. Veloso, and N. Uhlmann, "Energy resolving ct systems using medipix2 and MHSP detectors," *J. Instrum.*, vol. 8, Mar. 2013, Art. no. C03022.

[14] B. Meng, W. Cong, Y. Xi, B. De Man, J. Yang, and G. Wang, "Model and reconstruction of a k-edge contrast agent distribution with an X-ray photon-counting detector," *Opt. Express*, vol. 25, no. 8, pp. 9378–9392, 2017.

[15] R. Ewald, B. Brendel, K.-J. Engel, J.-P. Schlomka, A. Thran, and R. Proksa, "Sensitivity of photon-counting based K-edge imaging in X-ray computed tomography," *IEEE Trans. Med. Imag.*, vol. 30, no. 9, pp. 1678–1690, Sep. 2011.

[16] A. C. Thompson, H. D. Zeman, J. N. Otis, R. Hofstadter, E. Rubenstein, D. C. Harrison, R. S. Kernoff, J. C. Giacomini, H. J. Gordon, G. S. Brown, and W. Thomlinson, "Transvenous coronary angiography in dogs using synchrotron radiation," *Int. J. Cardiac Imag.*, vol. 2, no. 1, pp. 53–58, 1986.

[17] E. Schültke, S. Fiedler, C. Nemoz, L. Ogieglo, M. E. Kelly, P. Crawford, F. Esteve, T. Brochard, M. Renier, H. Requardt, G. Le Duc, B. Juurlink, and K. Meguro, "Synchrotron-based intra-venous k-edge digital subtraction angiography in a pig model: A feasibility study," *Eur. J. Radiol.*, vol. 73, no. 3, pp. 677–681, 2010.

[18] L. Sanghyeb, G. Jens, and O. Dustin, "Development and validation of a complete GATE model of the siemens inveon trimodal imaging platform," *Mol. Imag.*, vol. 12, no. 7, pp. 1–13, 2015.

[19] J. Allison, K. Amako, J. Apostolakis, H. Araujo, P. A. Dubois, M. Asai, G. Barrand, R. Capra, S. Chauvie, and R. Chytracek, "Geant4 developments and applications," *IEEE Trans. Nucl. Sci.*, vol. 53, no. 1, pp. 270–278, Feb. 2006.

[20] P. Rodrigues, R. Moura, C. Ortigao, L. Peralta, M. G. Pia, A. Trindade, and J. Varela, "Geant4 applications and developments for medical physics experiments," *IEEE Trans. Nucl. Sci.*, vol. 51, no. 4, pp. 1412–1419, Aug. 2004.

[21] C. J. Bateman *et al.*, "MARS-MD: Rejection based image domain material decomposition," vol. 13, May 2018, Art. no. P05020.
[22] J. H. Hubbell and S. M. Seltzer, "Tables of X-ray mass attenuation coefficients and mass energy-absorption coefficients 1 keV to 20 MeV for elements Z = 1 to 92 and 48 additional substances of dosimetric interest," *Pramana*, vol. 72, no. 2, pp. 375–387, 1995.
[23] M. F. Walsh, A. M. T. Opie, J. P. Ronaldson, R. M. N. Doesburg, S. J. Nik, J. L. Mohr, R. Ballabriga, A. P. H. Butler, and P. H. Butler, "First ct using medipix3 and the MARS-CT-3 spectral scanner," *J. Instrum.*, vol. 6, no. 1, 2011, Art. no. C01095.
[24] J. S. Butzer, "MARS-CT: Biomedical spectral X-ray imaging with medipix," Univ. Canterbury Phys. Astron., 2009.
[25] N. Ganet *et al.*, "Dosimetry for spectral molecular imaging of small animals with MARS-CT," *Med. Imag., Phys. Med. Imag. Int. Soc. Opt. Photon.*, 2015.

XIAOTONG ZHANG is currently pursuing the master's degree with the College of Medicine and Biological Information Engineering, Northeastern University. Her research interests include material decomposition based on spectral CT and CT image reconstruction methods.

DAYU XIAO received the master's degree in biomedical engineering from Northeastern University, in 2007, where he has been a Lecturer in biomedical engineering, since 2010. His current research interests include image reconstruction for X-ray cone-beam computed tomography and spectral CT.

YAN KANG received the bachelor's and master's degrees from Xi'an Jiaotong University, in 1987 and 1990, respectively, and the Ph.D. degree from the Institute of Medical Physics, University of Erlangen–Nuernberg, Germany, in 2002. He is currently the Vice President of Neusoft Medical Systems and the General Manager of the Clinical Application Business Unit. He was a Postdoctoral Scholar with the Laboratory of Image Guided Surgery, Stanford University, in 2004. He was the Ex-Dean of the Sino-Dutch Biomedical and Information Engineering School, Northeastern University, and the Director of Research Engineering Center for Medical Imaging and Intelligent Analysis, China Ministry of Education. He is the Chair of the Sub-Technique Commission of Medical Diagnostic Imaging Equipment, International Electro-Technical Commission (IEC/TC62B), and the China Standards Committee for Medical X-Ray Equipment and Devices. He holds 20 patents. He has authored or coauthored over 100 articles. He has published two books. His research interests include medical imaging, medical intelligent assistance, and computer simulations. He is a Committee Member of the National Education Guidance of Biomedical Engineering and the Executive Member of the National Medical Equipment Classification of CFDA. He is also a member of the RSNA and the RSE. He has also served as the Editor for the *Chinese Medical Equipment* journal.